CHEMISTRY OF MATERIALS

Article

pubs.acs.org/cm

Structure Tracking Aided Design and Synthesis of $Li_3V_2(PO_4)_3$ Nanocrystals as High-Power Cathodes for Lithium Ion Batteries

Liping Wang,[†,‡] Jianming Bai,[§] Peng Gao,[†,¶] Xiaoya Wang,[†,⊥] J. Patrick Looney,[†] and Feng Wang*[,†]

[†]Sustainable Energy Technologies Department and [§]National Synchrotron Light Source II, Brookhaven National Laboratory, Upton, New York 11973, United States

[‡]State Key Laboratory of Electronic Thin Films and Integrated Devices, School of Microelectronics and Solid-State Electronics, University of Electronic Science and Technology of China, Chengdu, Sichuan 610054, China

[⊥]Chemistry Department, Stony Brook University, Stony Brook, New York 11790, United States

Supporting Information

ABSTRACT: Preparing new electrode materials with synthetic control of phases and electrochemical properties is desirable for battery applications but hardly achievable without knowing how the synthesis reaction proceeds. Herein, we report on structure tracking-aided design and synthesis of single-crystalline $Li_3V_2(PO_4)_3$ (LVP) nanoparticles with extremely high rate capability. A comprehensive investigation was made to the local structural orderings of the involved phases and their evolution toward forming LVP phase using *in situ*/*ex situ* synchrotron X-ray and electron-beam diffraction, spectroscopy, and imaging techniques. The results shed light on the thermodynamics and kinetics of synthesis reactions and enabled the design of a cost-efficient synthesis protocol to make nanocrystalline LVP, wherein solvothermal treatment is a crucial step leading to an amorphous intermediate with local structural ordering resembling that of LVP, which, upon calcination at moderate temperatures, rapidly transforms into the desired LVP phase. The obtained LVP particles are about 50 nm, coated with a thin layer of amorphous carbon and featured with excellent cycling stability and rate capability − 95% capacity retention after 200 cycles and 66% theoretical capacity even at a current rate of 10 *C*. The structure tracking based method we developed in this work offers a new way of designing battery electrodes with synthetic control of material phases and properties.

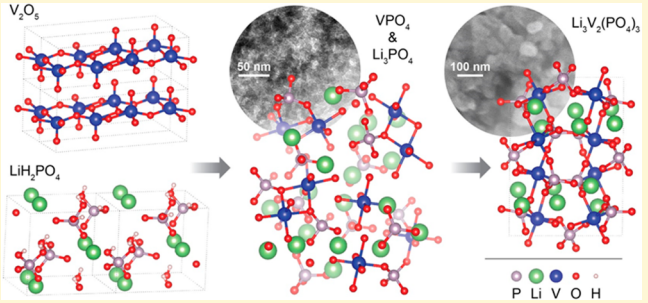

INTRODUCTION

Lithium-ion batteries (LIBs) are the preferred energy-storage devices for portable electronics and now are becoming one of the main power sources for electric vehicles and grids.[1] There has been considerable research interest in developing new electrode materials of high energy density and power density for use in next-generation batteries. Polyanion-type cathodes are of particular interest given the open while stable framework, as well as high voltage induced by phosphate groups and the possibility of accessing multiple redox states of transition metals particularly when vanadium is used (eventually enabling the high energy density). In addition to the traditional olivine-based metal phosphates (i.e., $LiMPO_4$; M = Fe, Mn), lithium vanadium phosphate, $Li_3V_2(PO_4)_3$ (LVP), has emerged as a promising cathode material due to its abundance, high thermal stability, and capability of delivering high capacity at high working potentials (~4 V).[2−5] Between the two polymorphs of LVP, i.e., rhombohedral and monoclinic phases,[6,7] the latter is thermodynamically stable and preferable for the use as high-energy and high-power cathodes owing to its three-dimensional open framework for fast lithium ion diffusion and accommodating up to 3 Li^+ (leading to a capacity of 197 $mAh{\cdot}g^{-1}$).[8]

A variety of methods were developed to obtain monoclinic LVP, including solid-state reaction,[9] sol gel,[4] microwave-assisted techniques,[10] hydrothermal/solvothermal or sol−gel assisted,[11−13] ionothermal synthesis,[14] and glass-ceramic processing.[15] The solvothermal route is environmentally benign and offers additional flexibility in controlling morphology, grain size, and *in situ* carbon coating and thus has been widely used for synthesizing $LiFePO_4$.[16] However, there are few reports on solvothermal synthesis of LVP,[11−13] and applying the method to tuning particle morphology remains a challenge due to the lack of understanding of the synthesis process. In this study, we explored solvothermal approaches for making monoclinic LVP, starting with investigating the synthesis reactions in a solvothermal environment. A combination of X-ray absorption spectroscopy (both near-edge structure (XANES) and extended fine structure (EXAFS)) of the V K-edge, *in situ* XRD, along with electron diffraction and high-resolution transmission electron microscopy (TEM) were applied to identify the local structural and chemical ordering in the

Received: June 14, 2015
Revised: July 30, 2015
Published: July 30, 2015

DOI: 10.1021/acs.chemmater.5b02236
Chem. Mater. 2015, 27, 5712−5718

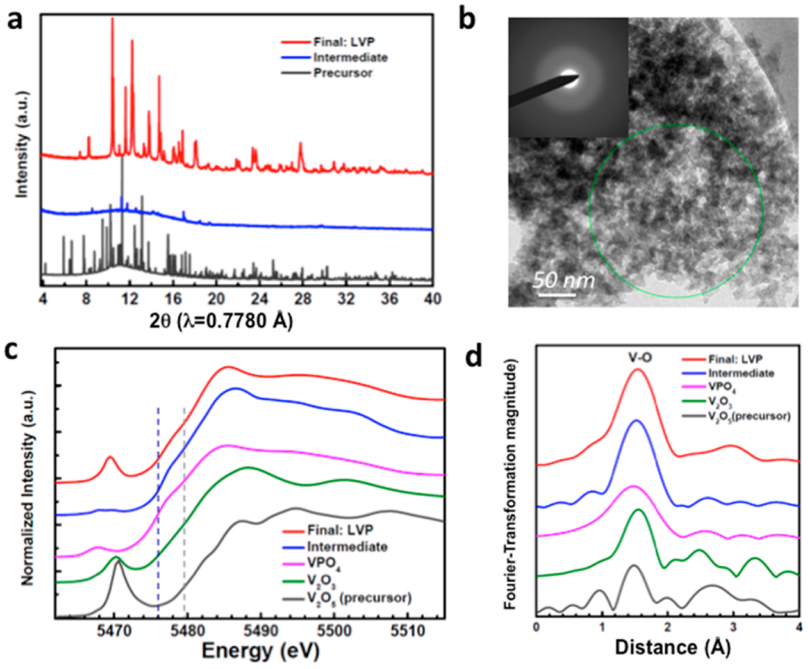

Figure 1. Structure of the intermediate and final phases in preparing monoclinic $Li_3V_2(PO_4)_3$ (LVP). (a) X-ray diffraction patterns of the precursor (black), intermediate phase (blue; with all the peaks associated with the Li_3PO_4 phase) and final phase (red), (b) bright-field TEM image and selected area electron-diffraction pattern (inset; recorded from the areas labeled by the green circle) of the intermediate phase, (c-d) XANES spectra and Fourier transformation magnitude of the EXAFS of V K-edge from intermediate (blue), final LVP (red), precursor V_2O_5 (gray), and reference compounds of VPO_4 (purple), and V_2O_3 (green). Vertical dashed lines were used to indicate the edge positions of the intermediate phase (blue) and precursor V_2O_5 (gray).

involved phases. The results from the investigation shed light on the kinetics and thermodynamics of synthesis reactions, indicating that solvothermal treatment is a crucial step leading to a VPO_4-like amorphous intermediate, which, upon calcination, transforms into the desired LVP phase. Through structure tracking to study the whole synthesis process, we were able to design a solvothermal-assisted protocol to synthesize single-crystalline LVP nanoparticles that exhibit excellent rate capability and cycling stability.

EXPERIMENTAL SECTION

Structure Tracking Using Synchrotron and TEM Techniques. The XRD measurements were performed at Beamline X14A, National Synchrotron Light Source, Brookhaven National Lab with a wavelength of 0.7780 Å. Rietveld refinements of the X-ray powder diffraction patterns were carried out using the GSAS/EXPGUI package. X-ray absorption spectroscopy (XAS) for the V K-edge was collected at Beamline X18A, National Synchrotron Light Source, Brookhaven National Laboratory. Energy calibration was established with the simultaneous absorption measurements on 5 μm-meter thick V metal foil inserted between the second and third ionization cell. TEM measurements were performed on a JEOL 2100F operated at 200 kV. The powder sample dispersed on a TEM grid (with an amorphous carbon-membrane support) were loaded on to a TEM holder and then transferred to the TEM column. TEM images and electron diffraction patterns were recorded by a charge-coupled device (CCD, Gatan).

***In Situ* XRD Measurements.** Similar to our previous report,[23] the intermediate phase after solvothermal treatment was placed in a quartz tube (about 0.7 mm inner diameter) filling about 2 mm of the tube. A small amount of quartz wool was inserted into the tube to keep the powders in place. The quartz tube was sealed with a one-end-capped Swagelok elbow under high pure Ar atmosphere in the glovebox. The XRD patterns were taken by 2°/step (2 theta from 4°−50°, about 6 min per pattern) with a heating rate 3 °C/min for the reactor. When the temperature reaches the point at which a pure LVP phase was obtained, the sample was held at that temperature, and the growth of LVP for a prolonged time was examined.

Synthesis of $Li_3V_2(PO_4)_3$. 0.015 mol of LiH_2PO_4 and 0.01 mol of V_2O_5 were added into 96 mL of ethylene glycol under magnetic stirring at 80 °C; subsequently, 1.7 g of sucrose was added into the yellow suspension. After vigorous stirring for 30 min, the blue solution was transferred into a Teflon vessel (120 mL) in a stainless steel autoclave. The autoclave was then purged with nitrogen, sealed, and placed in an oven at a constant temperature of 230 °C for 10 h. After the material was cooled to room temperature, the resulting brown suspension was stirred continuously to evaporate the solvent. Finally, the mixture was annealed in an inert atmosphere at 730 °C for 10 h. VPO_4-reference was obtained by ball milling the precursor V_2O_5, $NH_4H_2PO_4$, Li_2CO_3, and then this mixture was calcinated at 730 °C for 10 h under H_2/Ar atmosphere.

Electrochemical Measurements. The electrodes were prepared by casting slurry of 70 wt % active materials, 20 wt % Super-P carbon, and 10 wt % kynar binder on the Al foil. A Li foil was used as the counter electrodes. The electrolyte consisted of 1 M $LiPF_6$ dissolved in a mixture of ethylene carbonate (EC) and dimethyl carbonate (DMC) (1:1 by volume). Then, 2025-type coin cells were assembled in an argon-filled glovebox, and the galvanostatic charge−discharge performance was measured at different current rates using a VMP multipotentiostat.

RESULTS AND DISCUSSION

In the first step, the precursors LiH_2PO_4, V_2O_5, and sucrose in an ethylene glycol solution were heated in a sealed autoclave to high temperatures (typically 230 °C) for 10 h and then naturally cooled down to room temperature. A brown suspension was obtained and subsequently dried by continuously stirring (with solvent being evaporated). The product (hereon denoted as the intermediate phase) was a mixture of amorphous phases and Li_3PO_4 (JCPDS 15-0760) from

DOI: 10.1021/acs.chemmater.5b02236
Chem. Mater. 2015, 27, 5712−5718

precursors, identified from the tiny peaks in the XRD pattern shown in Figure 1a. TEM images (bright-field mode) and selected-area electron diffraction (SAED) patterns were also collected from local areas of the powders extracted from the intermediate product. The ill-defined particle morphology and presence of broadened diffusive rings in the SAED patterns (Figure 1b) further confirmed the amorphous nature of the intermediate.

The valence state of vanadium and short-range ordering in the intermediate phase were also examined via X-ray absorption spectroscopy. The oxidation state of vanadium was determined by X-ray absorption near-edge spectroscopy (XANES) of V K-edge (with V_2O_5 and V_2O_3 as references; Figure 1c). Overall, the energy position of the V K-edge from the intermediate phase is similar to that of V_2O_3, suggesting the reduction of the precursor V_2O_5 to a valence state close to 3+ after solvothermal treatment (with about a 3 eV chemical shift to a lower energy; indicated by the dotted lines). Considering that amorphous vanadium phosphorus oxide, VPO_4, was produced in a hydrothermal treatment,[17] and was ever used as an intermediate for the synthesis of $LiVPO_4F$[18] and $Li_5V(PO_4)_2F_2$,[19] we speculate that the amorphous component of the intermediate (after solvothermal treatment) is possibly a VPO_4-like phase. Thus, we synthesized amorphous VPO_4 powders using the solid-state reaction procedure as reported in the literature.[14] The XRD pattern was obtained from the resulting powder, showing that it is indeed amorphous (Figure S1). From the XAS measurements shown in Figure 1c, the XANES spectrum of the intermediate has a similar edge position and shape as that of the synthesized VPO_4. Also shown in Figure 1c, the XANES of the final product LVP resembles those of the intermediate and VPO_4 except for a prominent pre-edge peak around 5470 eV. The pre-edge peak originates from the dipole-forbidden transitions from 1s core levels to 3d states and is an indication of the distorted VO_6 octahedra in the LVP structure.[20] Figure 1d is a magnitude plot of the Fourier transformation of the extended X-ray absorption fine structure (FT-EXAFS) spectra for the V K-edge (k^3-weighted in k-space) of the intermediate phase, in comparison to that of the reference materials, including V_2O_3, V_2O_5, synthesized-VPO_4, and the final product LVP. In the FT-EXAFS of the LVP, there were two dominant peaks. The peak at approximately 1.5 Å is assigned to the single scattering-path from V to the closest oxygen atoms (the V−O bond in VO_6 octahedra), while the peak at R = ∼3.0 Å is attributed to the V−V bonding between two edge-sharing V−O_6 octahedra. It should be noted that the FT-EXAFS spectra are not phase-corrected and the actual bond lengths are longer. The FT-EXAFS of the intermediate phase also shows resemblance to that of LVP and synthesized VPO_4, with the first peak being present at about 1.5 Å (V−O bond in V−O_6 octahedra) (Figure 1d). The large-distance bonding (*i.e.*, V−V) is not shown in the FT-EXAFS of the intermediate and VPO_4 due to their amorphous nature. Therefore, the XAS spectra from these amorphous intermediates confirm that it assumes a similar valence state and local structure to that of VPO_4, as well as to the final LVP phase. According to the results from XRD, TEM, and XAS analysis, the intermediate is a Li−V−P−O composite containing a mixture of Li_3PO_4, the amorphous VPO_4-like phase, and carbon (derived from sucrose) as well. The chemical reaction during solvothermal synthesis at temperatures up to 230 °C presumably follows the route:

$$V_2O_5 + LiH_2PO_4 \rightarrow VPO_4 + Li_3PO_4 \quad (1)$$

Additional attempts were made to synthesize the crystalline LVP phase at even higher temperatures (up to 260 °C), but only amorphous intermediates were obtained (along with the residual Li_3PO_4). So it appears that calcination is needed to obtain the final LVP phase (as in Figure 1a). In order to obtain details of the structural evolution during calcination, *in situ* time-resolved XRD was performed during heating. The diffraction patterns were recorded every 14 min. Representative time-resolved XRD patterns were given in Figure 2a (see also

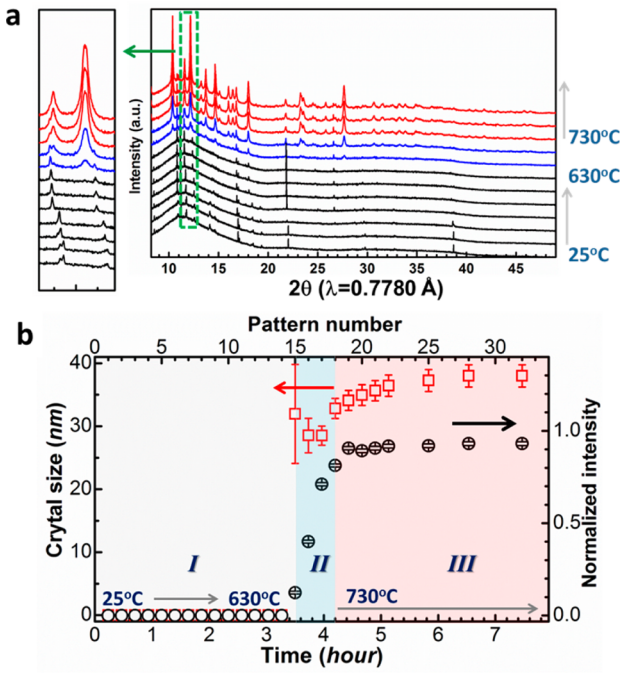

Figure 2. *Real time* tracking of the crystal growth of LVP during calcination by *in situ* XRD. (a) Time-resolved XRD patterns of the intermediate during heating from RT (25 °C) to 730 °C under an Ar atmosphere, (b) evolution of the crystal size (red square) and concentration of LVP (black circle) with time obtained from refinement of the XRD patterns, showing no formation of crystalline LVP below 630 °C, and rapid growth of LVP starting at 666 °C, followed with a slow growth during a prolonged time of constant-temperature heating at 730 °C.

Figure S2 for the index to some of the main peaks). In the early stage of heating (within the first ∼3.5 h), there was no visible change in the Bragg patterns until 630 °C, and thereafter the peaks associated with the Li_3PO_4 precursor began to disappear, and concomitant growth of new peaks associated with LVP phase became apparent. The diffraction peaks, being broad and weak due to nanocrystalline nature, became sharper and stronger with further heating (a trend more obvious in the expanded view in the inset). When the temperature reached 730 °C, pure phase of LVP was obtained, and no obvious change in the diffraction pattern was observed with further constant-temperature heating (730 °C).

In order to track the nucleation and growth processes of the LVP phase, we made refinements on individual XRD patterns, to obtain the width and intensity of the diffraction peaks, from which the particle size and the concentration of the LVP phase as a function of time and temperature were extracted, as shown in Figure 2b. In stage I (below 630 °C), no LVP was formed.

DOI: 10.1021/acs.chemmater.5b02236
Chem. Mater. 2015, 27, 5712−5718

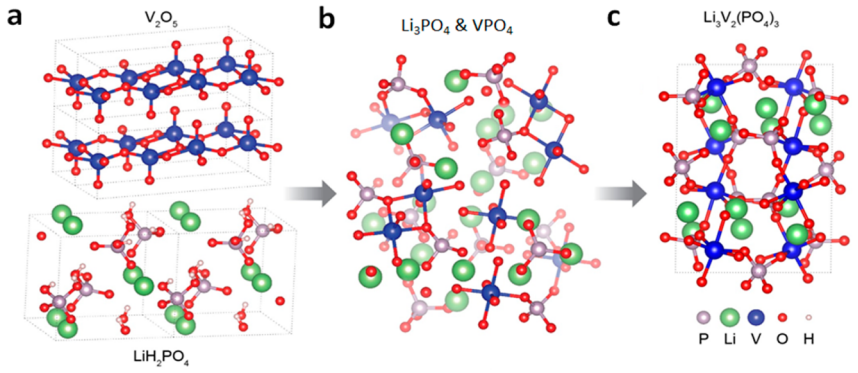

Figure 3. Local structural ordering during the solvothermal-assisted synthesis process, starting from (a) the precursor (V_2O_5, LiH_2PO_4), to (b) amorphous intermediate (VPO_4-like, Li_3PO_4), to (c) final monoclinic $Li_3V_2(PO_4)_3$ crystalline phase.

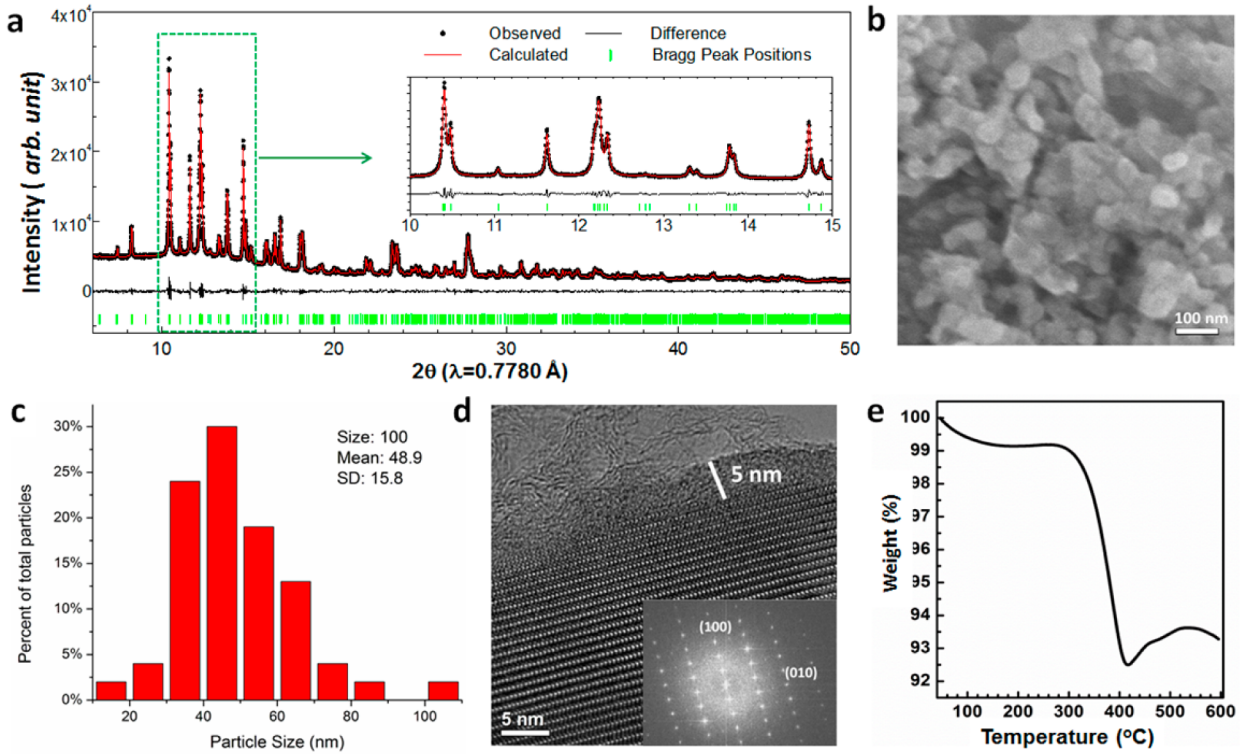

Figure 4. Structural properties of the synthesized LVP nanocrystals. (a) Synchrotron XRD pattern and Rietveld refinement with observed data points (red points), calculated data (black line), Bragg positions (green bars) for as-obtained LVP (R_{wp} = 2.81%, R_{exp}= 1.73%, R_p= 2.16%), (b) SEM image of LVP nanoparticles, (c) size distribution obtained from diameter measurements of 100 particles, (d) high- resolution TEM image and corresponding Fourier Transform (inset) of LVP, indicating its single-crystallinity, (e) thermogravimetric analyzer (TGA) curve of LVP during heating in air.

With further increase of temperature to about 666 °C (in Stage II), LVP particles, of about 30 nm, were formed rapidly, within the time needed to complete a single scan (14 min or less) although the concentration of LVP was still low. Interestingly, there was little change in the particle size as the temperature rose from 666 to 730 °C; while the concentration increased steadily, reaching the maximum value within 1 h. Since there is no growth of the particle size, the rapid increase in the concentration of the LVP must be due to the multiplication of the LVP nucleus at the current stage. During the prolonged heating in Stage III at 730 °C (>5 h), LVP concentration stayed almost constant and particle size became slightly larger, to about 40 nm, indicating that the growth of the LVP particles was largely hindered, most likely by the carbon coating on their surface since carbon was highly mixed with the V-containing phases in the intermediate.

As discussed above, solvothermal treatment is an essential step toward forming the VPO_4-like intermediate with a similar local ordering as LVP (Figure 1), both having VO_6 octahedra and PO_4 tetrahedra as building blocks (illustrated in Figure 3). As demonstrated in an earlier work,[21] the similarity in short-range order between the glassy precursor and the crystalline product promotes a bulk nucleation in silicate glasses. So we believe the local structural similarity between the VPO_4-like intermediate and LVP plays a critical role in the fast nucleation and growth of LVP nanocrystals.

In a recent report,[15] the glass-ceramic processing method was applied for fast synthesis of crystalline LVP. Contrary to their high temperature (1000 °C) melting step to generate the glassy

DOI: 10.1021/acs.chemmater.5b02236
Chem. Mater. 2015, 27, 5712−5718

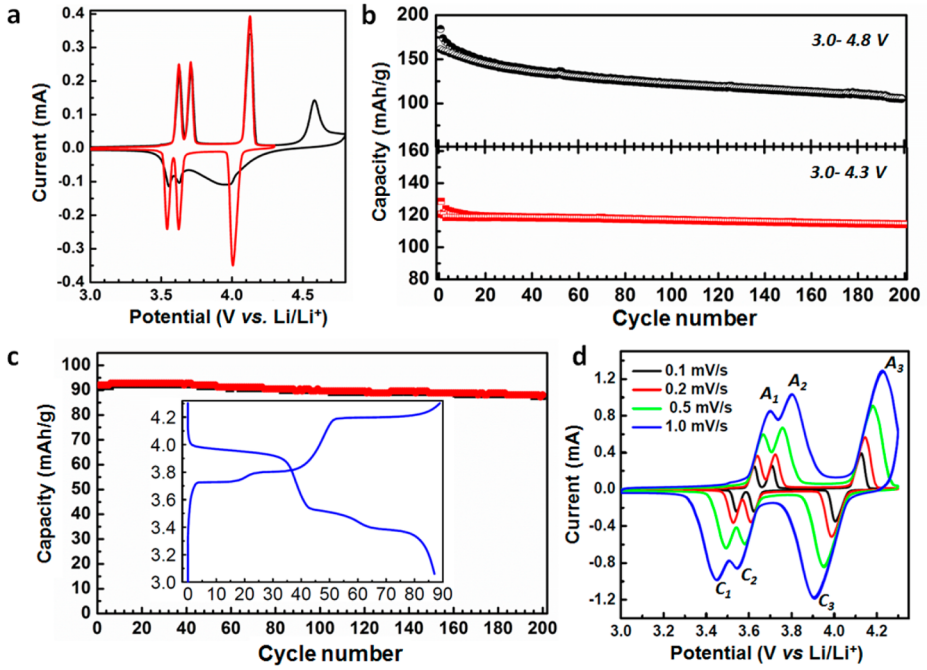

Figure 5. Electrochemical properties of LVP nanocrystals. (a) Cyclic voltammetry (CV) curves in the two different voltage windows of 3.0−4.8 V (black) and 3.0−4.3 V (red) at a scan rate of 0.1 mV·s^{-1}, (b) cycling performance in the windows of 3.0−4.8 V (black) and 3.0−4.3 V (red) at the current rate of 0.1 *C* for 200 cycles, (c) cycling performance and charge−discharge curve (inset) at 10 *C* in the window of 3.0−4.3 V, (d) evolution of the CV curves of LVP as a function of scan rates (from 0.1 to 10 mV·s^{-1}).

intermediate, our solvothermal treatment at mild temperature (230 °C) is much more cost-efficient; and importantly, the solvothermal step not only leads to the amorphous intermediate with desirable local ordering but also implements the reduction of the vanadium cations and the fine mixture of carbon, which are critical for producing the carbon-coated LVP nanocrystals.

Another important aspect in producing pure LVP is the processing of the intermediate during which the evaporation of the solvent after the solvothermal reaction was found to be critical in retaining stoichiometry. If only the solid powders were collected using filter papers after solvothermal treatment, impurities of V_2O_3 were found in the final product, likely due to the loss of the PO_4-containing components. The chemical reaction taking place in the calcination process presumably follows the route (2nd step shown in Figure 3):

$$2VPO_4 + Li_3PO_4 \rightarrow Li_3V_2(PO_4)_3 \quad (2)$$

Such a solvothermal-assisted synthetic process in producing LVP, namely solvothermal treatment followed with calcination, apparently differs from the one-pot solvothermal synthesis of the $LiFePO_4$ analogues.[20] However, our latest *in situ* investigation of the solvothermal synthesis of $LiFePO_4$, shows that a two-step, interface-coupled dissolution-reprecipitation process actually took place,[21] and the intermediate phase possesses a long-range ordering, with high resemblance to that of the final $LiFePO_4$. But during synthesis of LVP, the first step of solvothermal treatment only leads to an amorphous intermediate with short-range ordering, which is presumably due to the insufficiency of energy to activate the precipitation of LVP under solvothermal conditions (below 260 °C in our experiment). By combining the XAS, *in situ* XRD and TEM examinations of the structure of all the involved phases and their reorganization from the precursor (LiH_2PO_4, V_2O_5), to the intermediate (VPO_4, Li_3PO_4), and to the final phase ($Li_3V_2(PO_4)_3$), we were able to identify the whole reaction process, as illustrated in Figure 3.

Using the developed solvothermal-assisted synthetic protocol, i.e., solvothermal treatment at 230 °C followed by calcination at 730 °C, we obtained phase-pure LVP powders with a monoclinic structure (space group *P*21/*n*; cell parameters $\boldsymbol{a}$ = 8.6088(1) Å, $\boldsymbol{b}$ = 8.5985(1) Å, $\boldsymbol{c}$ = 12.0488(2) Å, $\boldsymbol{\beta}$ = 90.546(1)°) (Figure 4a). The crystallographic information and reliability from the refinements are given in the Supporting Information, Table S1. The particle size is highly uniform, about 50 nm in diameter, as examined by scanning electron microscopy (SEM; Figure 4b, c). These particles are single-crystalline and coated with amorphous carbon (less than 5 nm thick) according to high-resolution TEM image and Fast Fourier transform (Figure 4d). About 6.5 wt % of carbon in the powder was measured using thermogravimetric analyzer (TGA), by heating the materials in the air from RT to 600 °C (Figure 4e). This supports the observations from *in situ* XRD measurements, indicating that the presence of carbon that actually hindered the agglomeration and growth of the particles during calcinations, eventually leading to uniform size distribution of the LVP particles.

The as-obtained carbon-coated LVP particles were further assessed as cathodes in a half cell (with Li as counter electrodes). Figure 5a shows their cyclic voltammetry behavior in different voltage windows (3.0−4.3 and 3.0−4.8 V) at a scan rate of 0.1 mV·s^{-1}. During the charge process (lithium extraction) between 3.0−4.3 V, there are three obvious electrochemical signatures around 3.63, 3.71, and 4.13 V, which correspond to a series of phase transitions. Correspondingly, we observed three cathodic peaks at 4.0, 3.62, and 3.53 V during the discharge process (lithium reinsertion). Despite the similarity of overall cycling behaviors to earlier reports,[5,19] the CV curves show striking features of low polarization and sharp anodic and cathodic peaks, indicating the high electrochemical

DOI: 10.1021/acs.chemmater.5b02236
Chem. Mater. 2015, 27, 5712−5718

activity and fast reaction kinetics of the LVP electrodes. Nevertheless, the current peak at 4.58 V corresponding to extraction of the third lithium ($V^{4+} \rightarrow V^{5+}$) has a boarder shape with lower intensities, being consistent with previous reports.[8,24] Nazar et al.[24] ascribed this to the lower electronic/ionic conductivity of $V_2(PO_4)_3$, and, thus, it has slow reaction kinetics and low electrochemical activity. Interestingly, during the lithium reinsertion, in contrast to the lower voltage features, a solid solution behavior is initially observed with a characteristic S-shape curve. Subsequently, two electrochemical plateaus were observed at 3.63 and 3.55 V, respectively, and should be related to the reinsertion of the last lithium. This characteristic can be attributed to Li^+ disordering with the lack of V^{n+} ordering until sufficient Li^+ repopulation and the associating vanadium reduction takes place.[5]

The capacity-retention performances during 200 cycles are presented in Figure 5b. With full (de)lithiation between 3.0−4.8 V, it shows an initial charge-capacity of 186 mAh·g^{-1} (close to theoretical value, 197 mAh·g^{-1}), but there is a gradual fading of capacity during elongated cycling, to 105 mAh·g^{-1} after 200 cycles. This decline may reflect structural degradation during phase transition between $Li_{1.0}V_2(PO_4)_3$ and $V_2(PO_4)_3$[5] and the instability of the solid electrolyte interphase (SEI) formed above 4.5 V versus Li^+/Li.[3,25]Moreover, this could also be ascribed to formation of dendrite-like and granular lithium at the counter electrode lithium metal side,[26] which leads to inhomogeneous ionic and electronic conductivity in the cell.

When the operation voltage window is restricted to 3.0−4.3 V (with only 2 lithium being cycled) at the same current rate (19.7 mAh·g^{-1}), the cycling performance significantly improved, with only about 5% capacity decay after 200 cycles (from an initial discharge capacity of 120 mAh·g^{-1} to 114 mAh·g^{-1}). The rate performance was also tested via galvanostatic cycling at a current density of 1.33 A·g^{-1} (equivalent to 10 *C*) in Figure 5c and different charge−discharge current rates (Figure S3). It demonstrates negligible capacity decay, from initial 90 mAh·g^{-1} to 86 mAh·g^{-1} after 200 cycles. Such a rate performance of this carbon-coated LVP is remarkable and outperforms the micron-size C/LVP obtained via conventional solid-state reactions, in which a capacity of 80 mAh·g^{-1} at 1 *C* and capacity of 10 mAh·g^{-1} at 10 *C* was obtained (Figure S4a-c). On the other hand, the nanosized LVP has a much lower polarization in the charge−discharge curves even at such a high rate (inset of Figure 5c), which may be due to the small charge-transfer resistance (Figure S 4d).

The rate capability is among the best-performed LVP cathodes as reported in the literature.[4,9−15,22] For example, the capacity at 10 *C* is 2−3 times higher than that of the carbon-coated LVP synthesized via hydrothermal-assisted solid-state reactions (as being recently reported by Sun et al.),[11] where a discharge capacity of only 30 mAh·g^{-1} at 10 *C* was demonstrated. Such outstanding electrochemical performance may not be explained solely by enhanced electronic conductivity (with carbon coating) but also by the nanosize effect, particularly on minimizing the lithium transport route. We also applied CV techniques to estimate the lithium diffusion in the LVP electrodes (Figure 5d). The variation of peak current (I_p) is linear with the square root of the scanning rate ($v^{1/2}$), as shown in Figure S5. The apparent chemical-diffusion coefficient of lithium is about 10^{-10} cm^2·s^{-1} as determined by the Randles-Sevik equation (see details in the Supporting Information). It is 1 order of magnitude higher than the theoretical coefficient of lithium diffusion at room temperature (10^{-11} cm^2·s^{-1})[27] and 2−4 orders higher than that of traditional $LiFePO_4$ (10^{-14} cm^2·s^{-1})[28] and $LiNi_{0.5}Mn_{1.5}O_4$ (10^{-12} cm^2·s^{-1}), which may be explained by the three-dimensional lithium diffusion pathways, eventually leading to the high rate capacity.

CONCLUSIONS

In summary, aided by the structure tracking investigation of the synthesis reactions, we developed a solvothermal-assisted synthetic protocol for making monoclinic LVP nanocrystals, namely via solvothermal treatment, to obtain amorphous intermediate and subsequent calcination to get a pure LVP phase. Through X-ray absorption spectroscopy (XANES and EXAFS) and TEM imaging/diffraction studies was the local structural ordering, with high resemblance to that of final LVP phase, identified; while *in situ* XRD studies provided details of the crystal growth during calcination, revealing, for the first time, the rapid crystallization of LVP nanocrystals at a temperature as low as 666 °C. The results from this study also suggested that the one-pot synthesis of LVP in a low-temperature solvothermal environment may not be thermodynamically allowed.

The solvothermal-assisted protocol design was applied to the synthesis of carbon-coated single-crystalline LVP nanoparticles, which delivered excellent cycling retention with only about 5% capacity decay after 200 cycles. Good rate capability with a discharge capacity of 86 mAh·g^{-1} was also obtained in the voltage window 3.0−4.3 V at 10 *C* as a result of the surface carbon coating and nanosize that ensure a low charge-transfer resistance and a high lithium diffusion coefficient of 10^{-10} cm^2·s^{-1}.

ASSOCIATED CONTENT

Supporting Information

The Supporting Information is available free of charge on the ACS Publications website at DOI: 10.1021/acs.chemmater.5b02236.

Synthesis and XRD measurements of VPO_4 powder, rate performance of $Li_3V_2(PO_4)_3$/C at different rates, the morphology and electrochemistry of the micron-sized $Li_3V_2(PO_4)_3$ by solid-state reactions, diffusivity extraction from CV curves, and atomic sites of $Li_3V_2(PO_4)_3$ from refinement (PDF)

AUTHOR INFORMATION

Corresponding Author

*E-mail: fwang@bnl.gov.

Present Address

¶School of Physics, Peking University, Beijing 100871, China.

Notes

The authors declare no competing financial interest.

ACKNOWLEDGMENTS

We thank John Johnson, Steven Ehrlich, and Lihua Zhang for technical support and thank Tiffany Bowman for graphic design. This work is supported by the U.S. Department of Energy (DOE) Office of Energy Efficiency and Renewable Energy under the Advanced Battery Materials Research (BMR) program, Contract No. DE-SC0012704. P.G. was supported by the Laboratory Directed Research and Development (LDRD) program at Brookhaven National Laboratory, under Award No. 13-022. Research carried out at the Center for Functional

DOI: 10.1021/acs.chemmater.5b02236
Chem. Mater. 2015, 27, 5712−5718

Nanomaterials and the National Synchrotron Light Source, Brookhaven National Laboratory, was supported by the U.S. Department of Energy, Office of Basic Energy Sciences, under Contract No. DE-SC0012704.

REFERENCES

(1) Dunn, B.; Kamath, H.; Tarascon, J. M. Electrical Energy Storage for the Grid: A Battery of Choices. *Science* **2011**, *334*, 928−935.
(2) Padhi, A. K.; Nanjundaswamy, K. S.; Masquelier, C.; Goodenough, J. B. Mapping of transition metal redox energies in phosphates with NASICON structure by lithium intercalation. *J. Electrochem. Soc.* **1997**, *144*, 2581−2586.
(3) Goodenough, J. B.; Kim, Y. Challenges for Rechargeable Li Batteries. *Chem. Mater.* **2010**, *22*, 587−603.
(4) Huang, H.; Yin, S. C.; Kerr, T.; Taylor, N.; Nazar, L. F. Nanostructured composites: A high capacity, fast rate $Li_3V_2(PO_4)_3$/carbon cathode for rechargeable lithium batteries. *Adv. Mater.* **2002**, *14*, 1525−1528.
(5) Yin, S. C.; Grondey, H.; Strobel, P.; Anne, M.; Nazar, L. F. Electrochemical property: Structure relationships in monoclinic $Li_{3-y}V_2(PO_4)_3$. *J. Am. Chem. Soc.* **2003**, *125*, 10402−10411.
(6) Gaubicher, J.; Wurm, C.; Goward, G.; Masquelier, C.; Nazar, L. Rhombohedral form of $Li_3V_2(PO_4)_3$ as a cathode in Li-ion batteries. *Chem. Mater.* **2000**, *12*, 3240−3242.
(7) Lu, Y. H.; Wang, L.; Song, J.; Zhang, D. W.; Xu, M. W.; Goodenough, J. B. Aluminum-stabilized NASICON-structured $Li_3V_2(PO_4)_3$. *J. Mater. Chem. A* **2013**, *1*, 68−72.
(8) Kang, J.; Mathew, V.; Gim, J.; Kim, S.; Song, J.; Bin Im, W.; Han, J.; Lee, J. Y.; Kim, J. Pyro-synthesis of a high rate nano- $Li_3V_2(PO_4)_3$/C cathode with mixed morphology for advanced Li-ion batteries. *Sci. Rep.* **2014**, *4*, 4047.
(9) Sato, M.; Ohkawa, H.; Yoshida, K.; Saito, M.; Uematsu, K.; Toda, K. Enhancement of discharge capacity of $Li_3V_2(PO_4)_3$ by stabilizing the orthorhombic phase at room temperature. *Solid State Ionics* **2000**, *135* (1−4), 137−142.
(10) Mao, W. F.; Yan, J.; Xie, H.; Wu, Y.; Tang, Z. Y.; Xu, Q. A novel synthesis of $Li_3V_2(PO_4)_3$/C nanocomposite with excellent high-rate capacity and cyclability. *Mater. Res. Bull.* **2012**, *47*, 4527−4530.
(11) Sun, C. W.; Rajasekhara, S.; Dong, Y. Z.; Goodenough, J. B. Hydrothermal Synthesis and Electrochemical Properties of $Li_3V_2(PO_4)_3$/C-Based Composites for Lithium-Ion Batteries. *ACS Appl. Mater. Interfaces* **2011**, *3*, 3772−3776.
(12) Duan, W. C.; Hu, Z.; Zhang, K.; Cheng, F. Y.; Tao, Z. L.; Chen, J. $Li_3V_2(PO_4)_3$@C core-shell nanocomposite as a superior cathode material for lithium-ion batteries. *Nanoscale* **2013**, *5*, 6485−6490.
(13) Pei, B.; Jiang, Z. Q.; Zhang, W. X.; Yang, Z. H.; Manthiram, A. Nanostructured $Li_3V_2(PO_4)_3$ cathode supported on reduced graphene oxide for lithium-ion batteries. *J. Power Sources* **2013**, *239*, 475−482.
(14) Li, X. L.; He, W. X.; Xiao, Z. H.; Peng, F. F.; Chen, J. J. Ionothermal synthesis and rate performance studies of nanostructured $Li_3V_2(PO_4)_3$/C composites as cathode materials for lithium-ion batteries. *J. Solid State Electrochem.* **2013**, *17*, 1991−2000.
(15) Nagamine, K.; Honma, T.; Komatsu, T. A fast synthesis of $Li_3V_2(PO_4)_3$ crystals via glass-ceramic processing and their battery performance. *J. Power Sources* **2011**, *196*, 9618−9624.
(16) Popovic, J.; Demir-Cakan, R.; Tornow, J.; Morcrette, M.; Su, D. S.; Schlogl, R.; Antonietti, M.; Titirici, M. M. $LiFePO_4$ mesocrystals for lithium-ion batteries. *Small* **2011**, *7*, 1127−1135.
(17) Zheng, J. C.; Han, Y. D.; Zhang, B.; Shen, C.; Ming, L.; Ou, X.; Zhang, J. F. Electrochemical properties of VPO_4/C nanosheets and microspheres as anode materials for lithium-ion batteries. *ACS Appl. Mater. Interfaces* **2014**, *6*, 6223−6226.
(18) Qiao, X. C.; Yang, J. D.; Wang, Y. B.; Chen, Q. Q.; Zhang, T. T.; Liu, L.; Wang, X. Y. Electrochemical performance of $LiVPO_4F$/C composite cathode prepared through amorphous vanadium phosphorus oxide intermediate. *J. Solid State Electrochem.* **2012**, *16*, 1211−1217.
(19) Makimura, Y.; Cahill, L. S.; Iriyama, Y.; Goward, G. R.; Nazar, L. F. Layered lithium vanadium fluorophosphate, $Li_5V(PO4)_2F_2$: A 4 V class positive electrode material for lithium-ion batteries. *Chem. Mater.* **2008**, *20*, 4240−4248.
(20) Kuo, H. T.; Bagkar, N. C.; Liu, R. S.; Shen, C. H.; Shy, D. S.; Xing, X. K.; Lee, J.-F.; Chen, J. M. Structural Transformation of $LiVOPO_4$ to $Li_3V_2(PO_4)_3$ with enhanced capacity. *J. Phys. Chem. B* **2008**, *112*, 11250−11257.
(21) Mastelaro, R.; Zanotto, R. D.; Lequeux, N.; Cortes, R. Relationship between short-range order and ease of nucleation in $Na_2Ca_2Si_3O_9$, $CaSiO_3$ and $PbSiO_3$ glasses. *J. Non-Cryst. Solids* **2000**, *262*, 191−199.
(22) Wei, Q. L.; An, Q. Y.; Chen, D. D.; Mai, L. Q.; Chen, S. Y.; Zhao, Y. L.; Hercule, K. M.; Xu, L.; Minhas-Khan, A.; Zhang, Q. J. One-pot synthesized bicontinuous hierarchical $Li_3V_2(PO_4)_3$ mesoporous nanowires for high-rate and ultralong-life lithium-ion batteries. *Nano Lett.* **2014**, *14*, 1042−1048.
(23) Bai, J. M.; Hong, J.; Chen, H. Y.; Graetz, J.; Wang, F. Solvothermal Synthesis of $LiMnFePO_4$ Cathodes Materials: A Study of Reaction Mechanisms by Time-resolved In-situ Synchrotron X-Ray Diffraction. *J. Phys. Chem. C* **2015**, *119*, 2266−2276.
(24) Yin, S. C.; Strobel, P. S.; Grondey, H.; Nazar, L. F. Li2.5V2(PO4)(3): A room-temperature analogue to the fast-ion conducting high-temperature gamma-phase of $Li_3V_2(PO_4)_3$. *Chem. Mater.* **2004**, *16*, 1456−1465.
(25) Wang, L. P.; Li, H.; Huang, X. J.; Baudrin, E. A comparative study of Fd-3m and P4(3)32 "$LiNi_{0.5}Mn_{1.5}O_4$". *Solid State Ionics* **2011**, *193*, 32−38.
(26) Li, W.; Zheng, H.; Chu, G.; Luo, F.; Zheng, J.; Xiao, D.; Li, X.; Li, H.; Wei, X. Effect of electrochemical dissolution and deposition order on lithium dendrite formation: a top view investigation. *Faraday Discuss.* **2014**, *176*, 109−124.
(27) Lee, S.; Park, S. S. Atomistic Simulation Study of Monoclinic $Li_3V_2(PO_4)_3$ as a Cathode Material for Lithium Ion Battery: Structure, Defect Chemistry, Lithium Ion Transport Pathway, and Dynamics. *J. Phys. Chem. C* **2012**, *116*, 25190−25197.
(28) Tang, K.; Yu, X. Q.; Sun, J. P.; Li, H.; Huang, X. J. Kinetic analysis on $LiFePO_4$ thin films by CV, GITT, and EIS. *Electrochim. Acta* **2011**, *56*, 4869−4875.

DOI: 10.1021/acs.chemmater.5b02236
Chem. Mater. 2015, 27, 5712−5718